

# Nonlocal thermoelectric signature of helical edge states

Gianmichele Blasi,<sup>1,\*</sup> Fabio Taddei,<sup>1</sup> Liliana Arrachea,<sup>2</sup> Matteo Carrega,<sup>1</sup> and Alessandro Braggio<sup>1,†</sup>

<sup>1</sup>NEST, Scuola Normale Superiore and Istituto Nanoscienze-CNR, I-56126, Pisa, Italy

<sup>2</sup>International Center for Advanced Studies, ECyT-UNSAM,

Campus Miguelete, 25 de Mayo y Francia, 1650 Buenos Aires, Argentina

We consider a Josephson junction hosting a Kramer pair of helical edge states of a quantum spin Hall bar in contact with a normal-metal probe. In this hybrid system, the orbital phase induced by a small magnetic field threading the junction known as Doppler shift (DS), combines with the conventional Josephson phase difference and originates an effect akin to a Zeeman field in the spectrum. As a consequence, when a temperature bias is applied to the superconducting terminals, a thermoelectric current is established in the normal probe. We argue that this purely non-local thermoelectric effect is a unique signature of the helical nature of the edge states coupled to superconducting leads and it can constitute a useful tool for probing the helical nature of the edge states in systems where the Hall bar configuration is difficult to achieve. We fully characterize thermoelectric response and performance of this hybrid junction in a wide range of parameters, demonstrating that the external magnetic flux inducing the DS can be used as a knob to control the thermoelectric response and the heat flow in a novel device based on topological junctions.

*Introduction.*— Quantum spin Hall systems in two-dimensional topological insulators (TI) are receiving a lot of attention [1–4] due to their non-trivial topological properties. The clearest signature of the quantum spin Hall phase is the existence of Kramer pairs of helical edge states, which propagate in opposite directions with opposite spin orientations (spin-momentum locking). After the pioneering theoretical ideas [5–7] and experimental realizations in HgTe quantum wells [8–10], other platforms to realize this topological phase, preserving time-reversal symmetry, have been proposed in different materials [11–17]. In HgTe the helical nature of the edge states is commonly probed by means of nonlocal transport measurements in a Hall bar geometry with four or more terminals [8–10] and quantum point contacts [18–20]. This can be very hard to implement in some other systems, where evidence is shown on the existence of edge states but not yet on their helical nature [11–17].

When the Kramer pairs of helical edge states are embedded in a superconducting junction, the Andreev states inherit non-trivial properties. Topological Josephson junctions formed by two-dimensional TIs have been studied recently [21–32] and experimentally realized [33, 34]. In particular, a small magnetic flux in topological junctions can lead to very interesting features due to the effective orbital *Doppler shift* (DS) acquired by the electrons in the edge states [27].

In the present work we argue that the DS leads to a nonlocal thermoelectric effect as a unique consequence of the helical nature of the edge states. The setup under investigation is shown in Fig. 1(a), where a pair of edge states are contacted to superconductors, while a normal-metal probe – such as STM tip [35–38] – is directly contacted to the edge states. In the absence of DS, particle-hole symmetry, inherently present in superconducting systems, prevents the development of any thermoelectric effect. Remarkably, the DS has an effect akin to a Zeeman

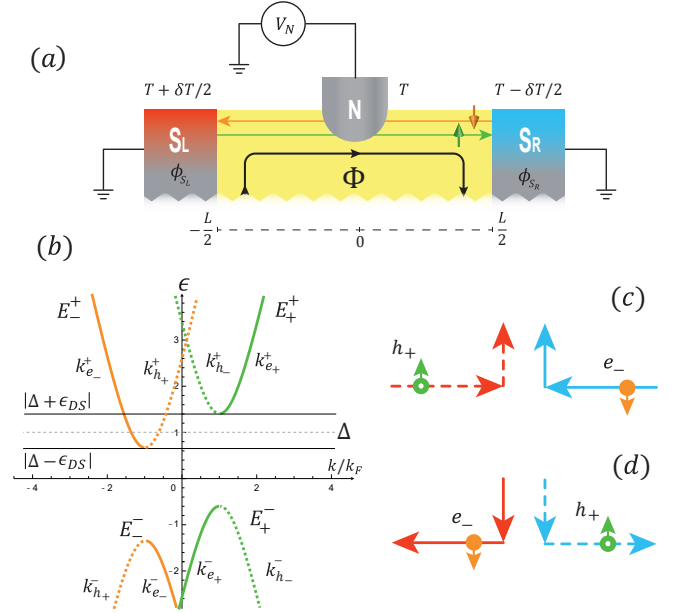


Figure 1. (a) Sketch of the setup. A helical Kramer pair of edge states of the quantum spin Hall effect is contacted by two superconductors at different temperatures,  $T_{S_L} = T + \delta T/2$  and  $T_{S_R} = T - \delta T/2$  and with a normal-metal probe at temperature  $T_N = T$  at which a bias voltage  $V_N$  is possibly applied. The structure is threaded by a magnetic flux which induces a Doppler shift in the edge states in addition to a Josephson phase difference applied between the two superconductors. (b) Dispersion curves for quasiparticles  $e_{\pm}$  (solid lines) and quasiholes  $h_{\pm}$  (dashed lines) in the proximized superconductor  $S_L/S_R$  for  $0 < \epsilon_{DS} < \Delta$ . Transport processes are depicted in panel (c) for  $V_N = 0, \delta T \neq 0$  and in panel (d) for  $V_N \neq 0, \delta T = 0$ , when the spectrum for  $e_+, h_-$  is assumed fully gapped.

man splitting in the two spin-polarized members of the Kramer pair. Although the whole system is particle-hole symmetric, the local density of states for each spin species

at the contact with the probe lack of symmetry between positive and negative energies due to the DS. Therefore, when a temperature difference is applied between the two superconductors a thermocurrent flows between the TI and the probe. The key for this response is the fact that the proximity to superconductors gives rise to a simultaneous flow of helical electrons and holes. Since they move in opposite directions, they thermalize with different reservoirs, see Fig. 1(c). The intrinsic particle-hole symmetry of a normal metal-superconducting junction can be broken, in order to generate thermoelectricity, by using a Zeeman field and spin-polarized barriers [39–41]. Our proposal, on the contrary, relies on a completely different mechanism which makes use of the helicity of the edge states under the effect of the DS. In the following we quantitatively discuss this peculiar effect in the linear response regime, using the scattering matrix approach. We analyse different figures of merit, and show that it is possible to achieve very high values of the nonlocal Seebeck coefficient.

*Model.*— We consider the topological Josephson junction depicted in Fig. 1(a) with the upper edge of length  $L$  tunnel coupled with a normal (N) probe. The width of the TI is assumed large such that upper and lower edges are decoupled, and thus we focus only on the former one. The two electrodes induce superconducting correlations on the edge states via proximity effect [27, 28]. The associated Bogoliubov-de Gennes (BdG) Hamiltonian reads

$$\mathcal{H} = \begin{pmatrix} H(x) & i\sigma_y \Delta(x) \\ -i\sigma_y \Delta(x)^* & -H(x)^* \end{pmatrix}, \quad (1)$$

where  $H(x) = v_F(-i\hbar\partial_x + p_{DS}/2)\sigma_z - \mu\sigma_0 + \Lambda(x)$  and  $-H(x)^*$  is its time-reversal partner. We include also a contact potential  $\Lambda(x) = \Lambda\delta(x+x_0) + \Lambda\delta(x-x_0)$  at the boundaries with  $x_0 = L/2$ ;  $v_F$  indicates Fermi velocity,  $\mu$  is the chemical potential and  $\sigma_i$  are the Pauli matrices. The momentum  $p_{DS} = (\pi\hbar/L)(\Phi/\Phi_0)$  represents the so-called doppler shift (DS) contribution describing the gauge invariant shift of momentum induced by a small magnetic flux  $\Phi$  through the TI junction [27]. We consider rigid boundary conditions for the order parameter  $\Delta(x) = \Delta[\Theta(-x-L/2)e^{i\phi_{S_L}} + \Theta(x-L/2)e^{i\phi_{S_R}}]$ , with  $\Theta(x)$  the step function and  $\phi_{S_L/S_R}$  the superconducting phase in the left/right superconductor, with gap amplitude  $\Delta$ .

The eigenspectrum of the BdG Hamiltonian is reported in Fig. 1(b) and is given by  $E_{\pm}^j(k) = (\epsilon_{DS} + j\sqrt{(\hbar v_F k \mp \mu)^2 + \Delta^2})$ , with  $j = \pm$  indicating branches with positive/negative concavity and  $\epsilon_{DS}(\Phi) = v_F p_{DS}/2$  being the Doppler-shift energy. The effect of the DS on the dispersion curve is to shift the various branches vertically by an amount  $\epsilon_{DS}$ , upwards or downwards, as shown in Fig. 1(b). A finite value of the magnetic flux  $\Phi$  reduces the gap, which closes when  $\epsilon_{DS}(\Phi) = \Delta$ . The quasiparticle (QP) eigenfunctions

in Nambu notation of both left/right superconductors ( $i = S_L, S_R$ ) are given by

$$\begin{aligned} \Psi_{e_+}^{i,j} &= \frac{1}{\sqrt{2\pi\hbar v_{e_+}^j}} (j u_- e^{i\frac{\phi_i}{2}}, 0, 0, v_- e^{-i\frac{\phi_i}{2}}) e^{ik_e^j x} \\ \Psi_{e_-}^{i,j} &= \frac{1}{\sqrt{2\pi\hbar v_{e_-}^j}} (0, -j u_+ e^{i\frac{\phi_i}{2}}, v_+ e^{-i\frac{\phi_i}{2}}, 0) e^{ik_e^j -x}, \end{aligned} \quad (2)$$

where

$$u_{\pm} = \sqrt{\frac{\Delta}{2\epsilon_{\pm}}} e^{\frac{1}{2}h(\epsilon_{\pm})}; \quad v_{\pm} = \sqrt{\frac{\Delta}{2\epsilon_{\pm}}} e^{-\frac{1}{2}h(\epsilon_{\pm})}$$

with  $\epsilon_{\pm} = \epsilon \pm \epsilon_{DS}$  and  $h(\epsilon_{\pm}) = \text{arcCosh}(\epsilon_{\pm}/\Delta)$  for  $\epsilon_{\pm} > \Delta$  and  $h(\epsilon_{\pm}) = i \arccos(\epsilon_{\pm}/\Delta)$  for  $\epsilon_{\pm} < \Delta$ . Here, the quasiparticle momentum is  $k_{e_{\pm}}^j = \pm k_F(j\sqrt{(\epsilon_{\mp}^2 - \Delta^2)/\mu^2 + 1})$  and  $v_{e_{\pm}}^j = \hbar^{-1}|\partial_k E_{\pm}| = v_F(u_{\mp}^j - v_{\mp}^j)$  is the associated group velocity. The quasi-hole (QH) eigenfunctions  $\Psi_{h_{\pm}}^{i,j}$  can be obtained by replacing  $(u_{\pm}, v_{\pm}) \rightarrow (v_{\pm}, u_{\pm})$ ,  $k_{e_{\pm}}^j \rightarrow k_{h_{\mp}}^j = k_{e_{\pm}}^{-j}$  and  $v_{e_{\pm}}^j \rightarrow v_{h_{\mp}}^j = v_{e_{\pm}}^j$  in Eq. (2). Finally, the tunnel coupling between the N probe and the edge states is described with a symmetric beamsplitter in terms of a spin-independent transmission amplitude  $t$ . Due to the helical nature of the TI, electrons injected through the probe with spin component collinear with the natural spin quantization axis of the TI edge propagate in one direction, while electrons with opposite spin component propagate in the other one.

Transport properties of this multiterminal system are determined using the scattering matrix formalism [42–44]. Our main focus here is the charge current flowing in the probe  $J_N^0$  and the heat current  $J_{S_L}^1$  flowing in the left superconducting lead  $S_L$ , in response to a small temperature gradient  $\delta T$  between the two superconductors  $T_{S_L/S_R} = T \pm \delta T/2$  and a voltage bias  $V_N$  applied to the N probe at temperature  $T_N = T$ . These currents can be written as [44]

$$\begin{aligned} J_i^k &= \frac{2}{h} \sum_j \sum_{\alpha,\beta} (\alpha\epsilon)^{1-k} \int_0^{\infty} d\epsilon (\epsilon - \mu_i)^k \\ &\quad \times \left( f_i^{\alpha}(\epsilon) - f_j^{\beta}(\epsilon) \right) P_{i,j}^{\alpha,\beta}(\epsilon), \end{aligned} \quad (3)$$

where  $k = 0$  stands for charge and  $k = 1$  for heat component and  $\alpha, \beta = \pm$  for QPs and QHs, respectively. The Fermi functions of the leads  $j = S_L, S_R, N$  are  $f_j^{\alpha}(\epsilon) = \{\exp[(\epsilon - \alpha\mu_j)/k_B T_j] + 1\}^{-1}$ , where  $\mu_N = eV_N$ ,  $\mu_{S_R} = \mu_{S_L} = 0$ , i.e. superconductors are grounded. The scattering coefficients  $P_{i,j}^{\alpha,\beta}$  represent the reflection ( $i = j$ ) or transmission ( $i \neq j$ ) probabilities of a quasiparticle of type  $\beta$  in lead  $j$  to a quasi-particle of type  $\alpha$  in lead  $i$  [42, 44]. It is worth to notice that from their explicit expressions there is no dependence of the scattering coefficients on the contact potential parameter  $\Lambda$ . This is a direct consequence of the helicity of the edge

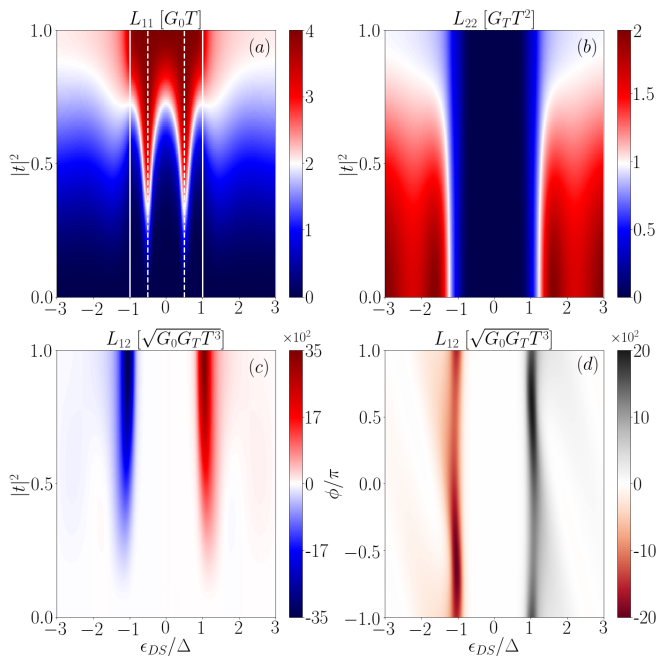


Figure 2. Onsager coefficients  $L_{11}$  (a),  $L_{22}$  (b) and  $L_{12} = -L_{21}$  (c) as functions of  $\epsilon_{DS}(\Phi)/\Delta$  and the coupling parameter  $|t|^2$  for phase bias  $\phi = \phi_{S_L} - \phi_{S_R} = 0$ ,  $T/T_C = 0.1$  and  $L/\xi = 1$ . (d)  $L_{12}$  as a function of  $\epsilon_{DS}(\Phi)/\Delta$  and the phase difference  $\phi$  for  $|t|^2 = 0.5$ . Such quantities are normalized as follows:  $L_{11}/(G_0T)$ ,  $L_{22}/(G_T T^2)$  and  $L_{12}/(\sqrt{G_0 G_T T^3})$ .

channels which do not admit ordinary reflections at the interfaces (i. e. Klein tunnelling [45]).

*Results.*— We now demonstrate and quantify the appearance of a nonlocal thermoelectric response due to the presence of a DS and the helical nature of the topological Josephson junction. We focus on linear response with  $V_N, \delta T \rightarrow 0$ . A simple physical picture of the thermoelectric mechanism can be grasped analyzing the dispersion-curves in Fig. 1(b). When  $\epsilon_{DS} > 0$ , left-moving (right-moving) QPs  $e_-$  (QHs  $h_+$ ) shift down with respect to the right-moving (left-moving) QPs  $e_+$  (QHs  $h_-$ ). For simplicity, we assume  $0 < (\Delta - \epsilon_{DS}(\Phi)) \sim k_B T \ll (\Delta + \epsilon_{DS}(\Phi))$  so that only left-moving QPs (right-moving QHs), thermalizing with the  $T_{S_R}$  ( $T_{S_L}$ ), contribute to the current. This unbalance between the fluxes of cold QPs and hot QHs [see Fig. 1(c)] leads to a thermocurrent flowing in the N probe. Moreover, it is worth to notice that, also in the non-linear regime, the thermocurrent does not depend explicitly on the probe's temperature as long as  $T_N \lesssim T$  in order to preserve the physical conditions of the device – see Ref. [42].

In addition to thermoelectricity, a  $\Phi$ -controlled non-local Peltier cooling may be also induced due to the application of a voltage  $V_N$ . In this case, as shown in Fig. 1(d), a charge current from the probe induces mainly left-moving QPs  $e_-$  and right-moving QHs  $h_+$  which determine a net energy transport from right to left between

the two superconductors even if they are kept at the same temperature. Notably, both the sign of the net thermoelectric current and the direction of the cooling can be varied by changing  $\Phi \rightarrow -\Phi$ . These conclusions are not affected by the Andreev bound states (ABSs), since they do not contribute neither to the thermal nor to the thermoelectrical transport processes.

Quantitatively, the linear response regime is characterized by the following relations [46–51]

$$\begin{aligned} J_N^0 &= L_{11}(V_N/T) + L_{12}(\delta T/T^2) \\ J_{S_L}^1 &= L_{21}(V_N/T) + L_{22}(\delta T/T^2), \end{aligned} \quad (4)$$

where  $V_N/T$  and  $\delta T/T^2$  are the thermodynamic forces (affinities). Notice that, although the configuration contains three terminals, the driving affinities are two. Hence, the Onsager matrix is effectively  $2 \times 2$  [46, 50–53]. Remarkably, in the present setup, the off-diagonal coefficients are nonlocal and satisfy the relation  $L_{12} = -L_{21}$ . The behavior of the Onsager coefficients  $L_{ij}$  ( $i, j = 1, 2$ ) are shown in Fig. 2 as functions of  $\epsilon_{DS}(\Phi)/\Delta$ . The diagonal and local coefficients  $L_{11}$  and  $L_{22}$  are plotted in units of  $G_0T$  and  $G_T T^2$ , while the nonlocal thermoelectrical coefficient  $L_{12}$  is plotted in units of  $\sqrt{G_0 G_T T^3}$ ; with  $G_0 = 2e^2/h$  and  $G_T = (\pi^2/3h)k_B^2 T$  being respectively the electrical conductance quantum and the thermal conductance quantum. In these plots, the length of the junction  $L$  is set equal to the superconducting coherence length  $\xi = \hbar v_F/(\pi\Delta)$ .

In Figs. 2(a) and (b) we plot  $L_{11}$  and  $L_{22}$ , respectively, as functions of  $\epsilon_{DS}(\Phi)/\Delta$  and  $|t|^2$ , setting  $\phi = \phi_{S_L} - \phi_{S_R} = 0$ . When the gap is open ( $|\epsilon_{DS}|/\Delta < 1$ ), and for low coupling  $|t|^2 \ll 1$ , the electrical conductance  $L_{11}/(G_0T)$  is almost zero apart from two sharp resonances located at  $\epsilon_{DS}/\Delta = \pm 1/2$ , where the ABSs cross zero-energy (indicated by white dashed lines in Figs. 2(a)) as expected in the tunneling limit [30]. By increasing the coupling  $|t|^2$  the resonances are broadened as a consequence of the enhancement of the effective linewidth of the ABSs. When  $|t|^2$  increases towards unity, the ABSs are spread and give rise to a finite electrical conductance in the whole range of values of  $\epsilon_{DS}$ , something that cannot be caught with a tunneling approach. For all values of  $|t|^2$  the thermal conductance  $L_{22}$  takes the largest values when the gap is closed  $|\epsilon_{DS}|/\Delta > 1$ , as one can see in Fig. 2(b). This is consistent with the fact that in the linear response regime the heat transport in a superconductor is mediated by quasiparticles [28, 29]. On the other hand,  $L_{22}$  vanishes within the gap when  $|\epsilon_{DS}|/\Delta < 1$ . This is due to the fact that ABSs cannot allow any thermal transport, while mediating the transport of charge through the Andreev reflection mechanism. When the gap is closed, the thermal conductance  $L_{22}$  presents small fluctuations as a consequence of interference effects and decreases at increasing coupling strength with the probe. In Fig. 2(c) we plot  $L_{12}$  as

a function of  $\epsilon_{DS}(\Phi)/\Delta$  and  $|t|^2$ , with  $\phi = 0$ . We distinguish two peaks at  $|\epsilon_{DS}(\Phi)| \sim \Delta$ . This is because in this condition the orange band (for  $\epsilon_{DS} \sim \Delta$ ) and the green band (for  $\epsilon_{DS} \sim -\Delta$ ) shown in Fig. 1(b) nearly touch zero energy, thus allowing a small temperature bias to drive a charge current even for a temperature  $k_B T \ll \Delta$ . The absolute value of  $L_{12}$  increases as a function of  $|t|^2$  and its sign changes when changing the sign of DS (or  $\Phi$ ). Fig. 2(d) visualizes the impact of the Josephson phase  $\phi$  (vertical axes) in the behavior of the nonlocal thermoelectric coefficient  $L_{12}$  for  $|t|^2 = 0.5$ . Here, we can notice that due to symmetry reasons  $L_{12}(\Phi, \phi) \rightarrow -L_{12}(-\Phi, -\phi)$ . As a final remark, when  $|t|^2 = 1$  (i. e. perfect coupling with the probe)  $L_{12}$  does not depend on the phase bias  $\phi$ .

To characterize the nonlocal effect induced by the DS we analyze the nonlocal Seebeck coefficient  $S = (1/T)L_{12}/L_{11}$  [51]. The latter is shown in Fig. 3, in units of  $\mu V/K$ , in the case of a weak coupling  $|t|^2 = 10^{-2}$ , where the Seebeck coefficient takes the highest values. In order to make realistic predictions in a wide temperature range, we have also included the self-consistent temperature behavior  $\Delta(T) = \Delta_0 \tanh(1.74\sqrt{T_C/T - 1})$ , accurate better than 2% with respect to the self-consistent BCS result [54, 55]. In Fig. 3(a) the Seebeck coefficient is reported at  $\phi = \pi/2$  for different values of temperatures: its peak value is quite high ( $\sim 65\mu V/K$ ), reaching the same order of magnitude of the values predicted for hybrid ferromagnetic-superconducting junctions [40, 56]. The maximum value of the Seebeck coefficient decreases by increasing the temperature  $T$  and it is reached at  $|\epsilon_{DS}| \sim \Delta(T)$ . The shape of  $S$  also depends on the phase bias  $\phi$  (see Fig. 3(b)); namely for  $\phi \neq 0$  it is not antisymmetric  $S(\phi, \Phi) \neq -S(\phi, -\Phi)$  with respect to  $\Phi$  while it becomes exactly antisymmetric for  $\phi = 0$ . For completeness, we analyze in the supplementary material [42] the figure of merit  $ZT$ . Remarkably, it reaches its maximum value for almost perfect coupling to the probe.

*Conclusions.*— We have discussed a striking consequence of the helical properties of the edge states in a topological Josephson junction in the presence of a normal metal probe coupled to one edge of a quantum spin Hall system. We showed that a thermal gradient between the superconductors in the presence of the Doppler shift generates a nonlocal thermoelectrical transport in the probe even in absence of any spin polarization. By using scattering matrix approach, we have quantitatively evaluated both local and nonlocal Onsager transport coefficients as a function of Doppler shift and phase difference. The nonlocal Seebeck coefficients can achieve high values, comparable with the best hybrid devices based on ferromagnetic elements, in the weak coupling limit (tunneling regime). These nonlocal features are a consequence of the spin-momentum locking of helical states and the induced Doppler shift which can be tuned by

means of small external magnetic fields. This additional knob can be used to tune the sign of the off-diagonal Onsager coefficient, and therefore to control heat and thermoelectric response in a topological Josephson junction based device. The present device is a very promising tool for probing the helical nature of the edge states in systems where the Hall bar configuration of edge states is difficult to realize.

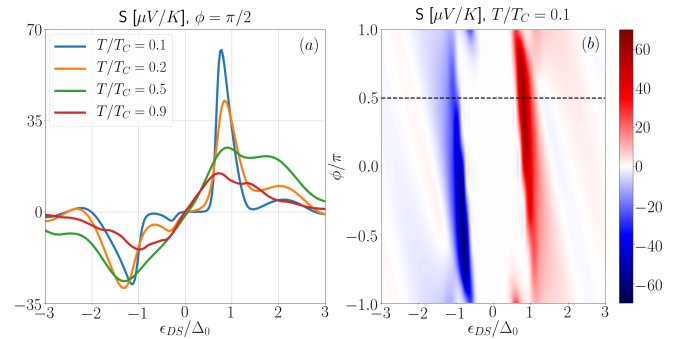


Figure 3. Seebeck coefficient as function of  $\epsilon_{DS}/\Delta_0$  for different temperatures at  $\phi = \pi/2$  (a) and as function of  $\epsilon_{DS}/\Delta_0$  and  $\phi$  for  $T/T_C = 0.1$  (b). The blue curve in panel (a) correspond to the cut at  $\phi = \pi/2$  of the Seebeck coefficient depicted in panel (b) (dashed line) obtained for the same set of parameters:  $L/\xi = 1$  and  $|t|^2 = 10^{-2}$ .

We acknowledge support from CNR-CONICET cooperation program “Energy conversion in quantum nanoscale hybrid devices”. We are sponsored by PIP-RD 20141216-4905 of CONICET, PICT-2014-2049 and PICT-2017-2726 from Argentina, as well as the Alexander von Humboldt Foundation, Germany (LA). A.B. and F.T. acknowledge SNS-WIS joint lab QUANTRA. M. C. is supported by the Quant-Era project “Supertop”. A. B. acknowledge the Royal Society through the International Exchanges between the UK and Italy (Grant No. IEC R2 192166).

\* [gianmichele.blasi@sns.it](mailto:gianmichele.blasi@sns.it)

† [alessandro.braggio@nano.cnr.it](mailto:alessandro.braggio@nano.cnr.it)

- [1] J. Moore, *Nature Phys* **5**, 378–380 (2009)
- [2] M. Z. Hasan and C. L. Kane *Rev. Mod. Phys.* **82**, 3045 (2010)
- [3] X-L. Qi, and S-C. Zhang, *Rev. Mod. Phys.* **83**, 1057 (2011).
- [4] Y. Ando, *Journal of the Physical Society of Japan* **82** 102001 (2013)
- [5] C. L. Kane and E. J. Mele, *Phys. Rev. Lett.* **95**, 146802 (2005).
- [6] C. L. Kane and E. J. Mele, *Phys. Rev. Lett.* **95**, 226801 (2005).
- [7] B. A. Bernevig, T. L. Hughes, and S.-C. Zhang, *Science* **314**, 1757 (2006).
- [8] M. König, S. Wiedmann, C. Brüne, A. Roth, H. Buh-

- mann, L. W. Molenkamp, X. L. Qi, and S-C. Zhang, *Science* **318**, 766 (2007).
- [9] A. Roth, C. Brüne, H. Buhmann, L. W. Molenkamp, J. Maciejko, X-L. Q, S-C Zhang, *Science* **325**, 294 (2009).
- [10] C. Brüne, A. Roth, H. Buhmann, E. M. Hankiewicz, L. W. Molenkamp, J. Maciejko, X-L. Qi, and S-C. Zhang, *Nature Phys.* **8**, 485 (2012).
- [11] Y. Shi, J. Kahn, Ben Niu, Zaiyao Fei, Bosong Sun, Xinghan Cai, Brian A. Francisco, Di Wu, Zhi-Xun Shen, Xiaodong Xu, David H. Cobden, and Yong-Tao Cui, *Science Adv.* **5** (2019)
- [12] S. Wu, V. Fatemi, Q. D. Gibson, K. Watanabe, T. Taniguchi, R. J. Cava, P. Jarillo-Herrero, *Science* **359**, 76 (2018).
- [13] S. Tang, C. Zhang, D. Wong, Z. Pedramrazi, H-Z Tsai, C. Jia, B. Moritz, M. Claassen, H. Ryu, S. Kahn, J. Jiang, H. Yan, M. Hashimoto, D. Lu, R. G. Moore, C-C. Hwang, C. Hwang, Z. Hussain, Y. Chen, M. M. Ugeda, Z. Liu, X. Xie, T. P. Devereaux, M. F. Crommie, S-K. Mo, and Z-X. Shen, *Nat. Phys.* **13**, 683 (2017).
- [14] Z-Y. Jia, Y-H. Song, X-B. Li, K. Ran, P. Lu, H-J. Zheng, X-Y. Zhu, Z-Q. Shi, J. Sun, J. Wen, D. Xing, and S-C. Li, *Phys. Rev. B* **96**, 41108 (2017).
- [15] F. Reis, G. Li, L. Dudy, M. Bauernfeind, S. Glass, W. Hanke, R. Thomale, J. Schäfer, R. Claessen, *Science* **357**, 21 (2017).
- [16] G. Li, W. Hanke, E. M. Hankiewicz, F. Reis, J. Schäfer, R. Claessen, C. Wu, R. Thomale, *Phys. Rev. B* **98**, 165146 (2018).
- [17] C. Liu, D. Culcer, M. T. Edmonds, M. S. Fuhrer, arXiv:1906.01214
- [18] R. Citro, F. Romeo, and N. Andrei *Phys. Rev. B* **84**, 161301 (2011)
- [19] F. Ronetti, L. Vannucci, G. Dolcetto, M. Carrega, M. Sasseti, *Phys. Rev. B* **93**(16), 165414 (2016).
- [20] F. Ronetti, M. Carrega, D. Ferraro, J. Rech, T. Jonckheere, T. Martin, M. Sasseti, *Phys. Rev. B*, **95**(11), 115412 (2017).
- [21] S. Barbarino, R. Fazio, M. Sasseti, F. Taddei, *New Journal of Physics*, **15**, 085025 (2013)
- [22] L. Fu and C. L. Kane, *Phys. Rev. B* **79**, 161408(R) (2009).
- [23] F. Dolcini, M. Houzet, and J. S. Meyer, *Phys. Rev. B* **92**, 035428 (2015)
- [24] S-P. Lee, K. Michaeli, J. Alicea, and A. Yacoby, *Phys. Rev. Lett.* **113**, 197001 (2014)
- [25] G. Tkachov, *Phys. Rev. B* **95**, 245407 (2017)
- [26] G. Blasi, F. Taddei, V. Giovannetti, and A. Braggio, *Phys. Rev. B* **99**, 064514 (2019)
- [27] Tkachov, G., Buset, P., Trauzettel, B., Hankiewicz, E. M., *Phys. Rev. B* **92**, 045408 (2015)
- [28] B. Sothmann and E. M. Hankiewicz, *Phys. Rev. B* **94**, 081407 (R), (2016).
- [29] B. Sothmann, F. Giazotto and E. M. Hankiewicz, *New J. Phys.* **19** 023056 (2017).
- [30] L. Bours, B. Sothmann, M. Carrega, E. Strambini, E. M. Hankiewicz, L. W. Molenkamp, and F. Giazotto, *Phys. Rev. Applied* **10**, 014027 (2018).
- [31] D. S. Shapiro, D. E. Feldman, A. D. Mirlin, and A. Shnirman, *Phys. Rev. B* **95**, 195425 (2017).
- [32] L. Bours, B. Sothmann, M. Carrega, E. Strambini, A. Braggio, E. M. Hankiewicz, L. W. Molenkamp, and F. Giazotto, *Phys. Rev. Applied* **11** 044073 (2019).
- [33] E. Bocquillon, R. S. Deacon, J. Wiedenmann, P. Leubner, T. M. Klapwijk, C. Brüne, K. Ishibashi, H. Buhmann, and L. W. Molenkamp, *Nature Nanotech.* **12**, 137 (2017)
- [34] J. Wiedenmann, E. Bocquillon, R. S. Deacon, S. Hartinger, O. Herrmann, T. M. Klapwijk, L. Maier, C. Ames, C. Brne, C. Gould, A. Oiwa, K. Ishibashi, S. Tarucha, H. Buhmann, and L. W. Molenkamp, *Nature Comm.* **7**, 10303 (2016).
- [35] S. Das, S. Rao, *Phys. Rev. Lett.* **106**, 236403 (2011).
- [36] L. Liu, A. Richardella, I. Garate, Y. Zhu, N. Samarth, and C. T. Chen, *Physical Review B*, **91**, 235437 (2015)
- [37] S. M. Hus, X. G. Zhang, G. D. Nguyen, W. Ko, A. P. Baddor, Y. P. Chen, and A. P. Li, *Phys. Rev. Lett.* **119**, 137202 (2017)
- [38] B. Voigtländer, V. Cherepanov, S. Korte, A. Leis, D. Cuma, S. Just, and F. Lüpke, *Review of Scientific Instruments*, **89**, 101101 (2018).
- [39] A. Ozaeta, P. Virtanen, F. S. Bergeret, and T. T. Heikkilä, *Phys. Rev. Lett.* **112**, 057001 (2014).
- [40] F. Sebastian Bergeret, M. Silaev, P. Virtanen, and T. T. Heikkilä, *Rev. Mod. Phys.* **90**, 041001 (2018).
- [41] F. Keidel, S-Y. Hwang, B. Trauzettel, B. Sothmann, P. Buset, arxiv:1907.00965
- [42] See supplemental material.
- [43] S. Datta, *Electronic Transport in Mesoscopic Systems* (Cambridge University Press, Cambridge, England, 1995).
- [44] C. J. Lambert and R. Raimondi, *J. Phys. Condens. Matter* **10**, 901 (1998)
- [45] S. Lee, V. Stanev, X. Zhang et al., *Nature* **570**, 344–348 (2019)
- [46] F. Mazza, R. Bosisio, G. Benenti, V. Giovannetti, R. Fazio and F. Taddei, *New J. Phys.* **16**, 085001 (2014).
- [47] R. Sánchez, P. Buset, and A. Levy Yeyati, *Phys. Rev. B* **98**, 241414(R) (2018)
- [48] R. Hussein, M. Governale, S. Kohler, W. Belzig, F. Giazotto, and A. Braggio, *Phys. Rev. B* **99**, 075429 (2019)
- [49] N. S. Kirsanov, Z. B. Tan, D. S. Golubev, P. J. Hakonen, and G. B. Lesovik, *Phys. Rev. B* **99**, 115127 (2019)
- [50] P. Roura-Bas, L. Arrachea, and E. Fradkin, *Phys. Rev. B* **98**, 195429 (2018).
- [51] G. Benenti, G. Casati, K. Saito, R. S. Whitney, *Phys. Rep.* **694**, 1 (2017).
- [52] R. Sánchez, B. Sothmann, A. N. Jordan, *Phys. Rev. Lett.* **114**, 146801 (2015).
- [53] Mani, A., Benjamin, C., *Phys. Rev. E* **97**(2), 022114 (2018).
- [54] M. Kamp, B. Sothmann, *Phys. Rev. B* **99**, 045428 (2019)
- [55] Tinkham, M., *Introduction to superconductivity* (McGraw-Hill, New York, 1996)
- [56] F. Giazotto, P. Solinas, A. Braggio, and F.S. Bergeret, *Phys. Rev. Applied* **4**, 044016 (2015).

## SUPPLEMENTARY MATERIAL

### SCATTERING MATRIX

Here, we determine the full scattering matrix of the setup depicted in Fig. 1(a) of the main text. We start considering the scattering problem associated to the topological Josephson junction, evaluating the scattering matrix coefficients at the interface between superconducting leads ( $S_L/S_R$ ) and the upper edge state of the TI. In order to do that, let us start by considering the case of an incident spin-up electron, incoming from the TI towards the interface with the right superconductor  $S_R$ . The incoming wave reflects back into the TI region in a left-moving spin-down electron or a left-moving spin-down hole; while into the superconducting region it transmits (if the energy is above the gap) as a right-moving spin-up electron-like or a right-moving spin-up hole-like quasi-particle:

$$\Psi_{e_+}^{TI}(x_0^-) + r_{ee}^R \Psi_{e_-}^{TI}(x_0^-) + r_{he}^R \Psi_{h_-}^{TI}(x_0^-) = t_{\tilde{e}e}^R \Psi_{e_+}^{S_R,j}(x_0^+) + t_{\tilde{h}e}^R \Psi_{h_+}^{S_R,j}(x_0^+) \quad (\text{S.5})$$

In that case  $x_0^\pm = \lim_{\delta \rightarrow 0^\pm} x_0 + \delta$  with  $x_0 = L/2$ . Similar equations can be found for incoming holes, QPs and QHs at both the interfaces. In Eq. (S.5) (and similar)  $\Psi_{e_\pm}^{TI}$  and  $\Psi_{h_\pm}^{TI}$  represent the right/left-moving electrons/holes eigenfunctions in the  $TI$ ; while  $\Psi_{e_\pm}^{i,j}$  and  $\Psi_{h_\pm}^{i,j}$  represent the right/left-moving QPs/QHs eigenfunctions in the  $i = S_L, S_R$  superconductor (as reported in Eq. (2) of the main text). The coefficients  $r_{\alpha,\beta}^{L/R}$  and  $t_{\alpha,\beta}^{L/R}$  represent respectively the reflection and transmission amplitudes of an incoming particle of type  $\beta$  to a particle of type  $\alpha$  at the left/right interface. Here we indicate with  $\{\alpha, \beta\} = \{e, h\}$  electrons and holes in the  $TI$  and with  $\{\alpha, \beta\} = \{\tilde{e}, \tilde{h}\}$  QPs and QHs in the superconductors.

In order to find the solutions for the scattering amplitudes of Eqs. (S.5) we have to impose the boundary condition obtained by integrating the BdG equation (see Eq. 1 in the main text):

$$\begin{cases} -\lambda^* u_\uparrow(x_0^-) = -\lambda u_\uparrow(x_0^+) \\ \lambda u_\downarrow(x_0^-) = \lambda^* u_\downarrow(x_0^+) \\ -\lambda v_\uparrow(x_0^-) = -\lambda^* v_\uparrow(x_0^+) \\ \lambda^* v_\downarrow(x_0^-) = \lambda v_\downarrow(x_0^+) \end{cases} \quad (\text{S.6})$$

where  $\lambda = 1 + i \frac{\Delta}{2\epsilon_F}$  and  $x_0 = \pm \frac{L}{2}$ . The explicit solution of the linear set of equations (Eq. (S.5) and similar) with the boundary conditions of Eq. (S.6), leads to the following scattering amplitudes for the left

$$x_0 = -\frac{L}{2} \left\{ \begin{array}{l} r_{he}^L = -\frac{v_+}{u_+} e^{i\alpha_+} e^{-i\phi_L} \\ r_{eh}^L = \frac{v_-}{u_-} e^{i\alpha_-} e^{i\phi_L} \\ r_{\tilde{h}\tilde{e}}^L = -\frac{v_-}{u_-} e^{-i\beta_-} \cdot \Theta(|\epsilon_-| - \Delta) \\ r_{\tilde{e}\tilde{h}}^L = -\frac{v_+}{u_+} e^{-i\beta_+} \cdot \Theta(|\epsilon_+| - \Delta) \end{array} \right. \quad \begin{array}{l} t_{\tilde{e}e}^L = -\frac{\lambda^* \sqrt{u_+^2 - v_+^2}}{\lambda u_+} e^{\frac{i}{2}(\alpha_+ - \beta_+)} e^{-i\frac{\phi_L}{2}} \cdot \Theta(|\epsilon_+| - \Delta) \\ t_{\tilde{h}h}^L = \frac{\lambda \sqrt{u_-^2 - v_-^2}}{\lambda^* u_-} e^{\frac{i}{2}(\alpha_- - \beta_-)} e^{i\frac{\phi_L}{2}} \cdot \Theta(|\epsilon_-| - \Delta) \\ t_{e\tilde{e}}^L = \frac{\lambda^* \sqrt{u_-^2 - v_-^2}}{\lambda u_-} e^{\frac{i}{2}(\alpha_- - \beta_-)} e^{i\frac{\phi_L}{2}} \cdot \Theta(|\epsilon_-| - \Delta) \\ t_{h\tilde{h}}^L = \frac{\lambda \sqrt{u_+^2 - v_+^2}}{\lambda^* u_+} e^{\frac{i}{2}(\alpha_+ - \beta_+)} e^{-i\frac{\phi_L}{2}} \cdot \Theta(|\epsilon_+| - \Delta) \end{array}$$

and the right interface

$$x_0 = \frac{L}{2} \left\{ \begin{array}{l} r_{he}^R = \frac{v_-}{u_-} e^{i\alpha_-} e^{-i\phi_R} \\ r_{eh}^R = -\frac{v_+}{u_+} e^{i\alpha_+} e^{i\phi_R} \\ r_{\tilde{h}\tilde{e}}^R = -\frac{v_+}{u_+} e^{-i\beta_+} \cdot \Theta(|\epsilon_+| - \Delta) \\ r_{\tilde{e}\tilde{h}}^R = -\frac{v_-}{u_-} e^{-i\beta_-} \cdot \Theta(|\epsilon_-| - \Delta) \end{array} \right. \quad \begin{array}{l} t_{\tilde{e}\tilde{e}}^R = \frac{\lambda^*}{\lambda} \frac{\sqrt{u_-^2 - v_-^2}}{u_-} e^{\frac{i}{2}(\alpha_- - \beta_-)} e^{-i\frac{\phi_R}{2}} \cdot \Theta(|\epsilon_-| - \Delta) \\ t_{\tilde{h}\tilde{h}}^R = \frac{\lambda}{\lambda^*} \frac{\sqrt{u_+^2 - v_+^2}}{u_+} e^{\frac{i}{2}(\alpha_+ - \beta_+)} e^{i\frac{\phi_R}{2}} \cdot \Theta(|\epsilon_+| - \Delta) \\ t_{e\tilde{e}}^R = -\frac{\lambda^*}{\lambda} \frac{\sqrt{u_+^2 - v_+^2}}{u_+} e^{\frac{i}{2}(\alpha_+ - \beta_+)} e^{i\frac{\phi_R}{2}} \cdot \Theta(|\epsilon_+| - \Delta) \\ t_{h\tilde{h}}^R = \frac{\lambda}{\lambda^*} \frac{\sqrt{u_-^2 - v_-^2}}{u_-} e^{\frac{i}{2}(\alpha_- - \beta_-)} e^{-i\frac{\phi_R}{2}} \cdot \Theta(|\epsilon_-| - \Delta) \end{array}$$

While, when  $|\epsilon_{DS}| > \Delta$ , for  $0 < \epsilon < |\Delta - |\epsilon_{DS}||$ , hold the following relations for the left

$$x_0 = -\frac{L}{2} \left\{ \begin{array}{l} r_{he}^L = -\frac{v_+}{u_+} e^{i\alpha_+} e^{-i\phi_L} \\ r_{eh}^L = -\frac{v_-}{u_-} e^{i\alpha_-} e^{i\phi_L} \\ r_{\tilde{h}\tilde{e}}^L = -\frac{v_-}{u_-} e^{i\beta_-} \\ r_{\tilde{e}\tilde{h}}^L = -\frac{v_+}{u_+} e^{-i\beta_+} \end{array} \right. \quad \begin{array}{l} t_{\tilde{e}\tilde{e}}^L = -\frac{\lambda^*}{\lambda} \frac{\sqrt{u_+^2 - v_+^2}}{u_+} e^{\frac{i}{2}(\alpha_+ - \beta_+)} e^{-i\frac{\phi_L}{2}} \\ t_{\tilde{h}\tilde{h}}^L = \frac{\lambda}{\lambda^*} \frac{\sqrt{u_-^2 - v_-^2}}{u_-} e^{\frac{i}{2}(\alpha_- + \beta_-)} e^{i\frac{\phi_L}{2}} \\ t_{e\tilde{e}}^L = -\frac{\lambda^*}{\lambda} \frac{\sqrt{u_-^2 - v_-^2}}{u_-} e^{\frac{i}{2}(\alpha_- + \beta_-)} e^{i\frac{\phi_L}{2}} \\ t_{h\tilde{h}}^L = \frac{\lambda}{\lambda^*} \frac{\sqrt{u_+^2 - v_+^2}}{u_+} e^{\frac{i}{2}(\alpha_+ - \beta_+)} e^{-i\frac{\phi_L}{2}} \end{array}$$

and the right interface

$$x_0 = \frac{L}{2} \left\{ \begin{array}{l} r_{he}^R = -\frac{v_-}{u_-} e^{i\alpha_-} e^{-i\phi_R} \\ r_{eh}^R = -\frac{v_+}{u_+} e^{i\alpha_+} e^{i\phi_R} \\ r_{\tilde{h}\tilde{e}}^R = -\frac{v_+}{u_+} e^{-i\beta_+} \\ r_{\tilde{e}\tilde{h}}^R = -\frac{v_-}{u_-} e^{i\beta_-} \end{array} \right. \quad \begin{array}{l} t_{\tilde{e}\tilde{e}}^R = -\frac{\lambda^*}{\lambda} \frac{\sqrt{u_-^2 - v_-^2}}{u_-} e^{\frac{i}{2}(\alpha_- + \beta_-)} e^{-i\frac{\phi_R}{2}} \\ t_{\tilde{h}\tilde{h}}^R = \frac{\lambda}{\lambda^*} \frac{\sqrt{u_+^2 - v_+^2}}{u_+} e^{\frac{i}{2}(\alpha_+ - \beta_+)} e^{i\frac{\phi_R}{2}} \\ t_{e\tilde{e}}^R = -\frac{\lambda^*}{\lambda} \frac{\sqrt{u_+^2 - v_+^2}}{u_+} e^{\frac{i}{2}(\alpha_+ - \beta_+)} e^{i\frac{\phi_R}{2}} \\ t_{h\tilde{h}}^R = \frac{\lambda}{\lambda^*} \frac{\sqrt{u_-^2 - v_-^2}}{u_-} e^{\frac{i}{2}(\alpha_- + \beta_-)} e^{-i\frac{\phi_R}{2}} \end{array}$$

in which

$$\alpha_{\pm} = \frac{\epsilon \pm \epsilon_{DS}}{\epsilon_c}; \quad \beta_{\pm} = \frac{\sqrt{(\epsilon \pm \epsilon_{DS})^2 - \Delta^2}}{\epsilon_c} \quad (\text{S.7})$$

with  $\epsilon_c = \frac{\hbar v_F}{L}$  is the confining energy. In the above expressions we focused on positive energies  $\epsilon \geq 0$  since in the expression of the currents (reported in Eq. (S.13)) the integration is performed over  $\epsilon \in [0, \infty[$ . Now, we consider the full system with the normal probe tunnel coupled to the upper edge of the TI. The full scattering matrix in Nambu space is

$$\Psi_{(i,a)}^{\alpha} |out\rangle = S_{(i,a)(j,b)}^{\alpha\beta} \Psi_{(j,b)}^{\beta\eta} |in\rangle \quad (\text{S.8})$$

between incoming/outgoing states  $(j,b)/(i,a)$  with leads indices are  $i, j = \text{N}, \text{S}_L, \text{S}_R$  with the channels labelled by  $a, b$ . In particular we assume a symmetric beam splitter which describes the contact interface between the normal lead N and the TI. The beam splitter is characterized by a reflectance and transmittance amplitudes

$$r = \cos(\eta) \quad \text{and} \quad t = i \sin(\eta) \quad (\text{S.9})$$

which depend on only one parameter  $\eta \in [0, \frac{\pi}{2}]$ . By taking into account the scattering amplitudes at the interfaces with the superconductors obtained above we get the full scattering matrix of the system:

$$\begin{pmatrix} c_{N\downarrow}^\downarrow \\ c_{N\uparrow}^\downarrow \\ c_{S_L\downarrow}^\downarrow \\ c_{S_R\uparrow}^\downarrow \\ b_{N\downarrow}^\downarrow \\ b_{N\uparrow}^\downarrow \\ b_{S_L\downarrow}^\downarrow \\ b_{S_R\uparrow}^\downarrow \end{pmatrix}_{out} = \begin{pmatrix} 0 & a_2 & 0 & a_4 & C_1 & 0 & C_3 & 0 \\ a_1 & 0 & a_3 & 0 & 0 & C_2 & 0 & C_4 \\ 0 & b_2 & 0 & b_4 & D_1 & 0 & D_3 & 0 \\ b_1 & 0 & b_3 & 0 & 0 & D_2 & 0 & D_4 \\ A_1 & 0 & A_3 & 0 & 0 & c_2 & 0 & c_4 \\ 0 & A_2 & 0 & A_4 & c_1 & 0 & c_3 & 0 \\ B_1 & 0 & B_3 & 0 & 0 & d_2 & 0 & d_4 \\ 0 & B_2 & 0 & B_4 & d_1 & 0 & d_3 & 0 \end{pmatrix}_S \begin{pmatrix} c_{N\downarrow}^\uparrow \\ c_{N\uparrow}^\uparrow \\ c_{S_L\downarrow}^\uparrow \\ c_{S_R\uparrow}^\uparrow \\ b_{N\downarrow}^\uparrow \\ b_{N\uparrow}^\uparrow \\ b_{S_L\downarrow}^\uparrow \\ b_{S_R\uparrow}^\uparrow \end{pmatrix}_{in} \quad (\text{S.10})$$

where

$$\begin{aligned} a_1 &= r + \frac{r_{eh}^L r_{he}^R t^2 r^*}{1 - r_{eh}^L r_{he}^R |r|^2}; & a_2 &= \frac{r_{eh}^R r_{he}^L t^2 r^*}{1 - r_{eh}^R r_{he}^L |r|^2} + r; & a_3 &= \frac{tt^L_{eE}}{1 - r_{eh}^L r_{he}^R |r|^2}; & a_4 &= \frac{tt^R_{eE}}{1 - r_{eh}^R r_{he}^L |r|^2}; \\ b_1 &= \frac{tt^R_{\bar{e}e}}{1 - r_{eh}^R r_{he}^L |r|^2}; & b_2 &= \frac{tt^L_{\bar{e}e}}{1 - r_{eh}^L r_{he}^R |r|^2}; & b_3 &= \frac{rt^L_{e\bar{e}} t^R_{\bar{e}e}}{1 - r_{eh}^L r_{he}^R |r|^2}; & b_4 &= \frac{rt^R_{\bar{e}e} t^L_{e\bar{e}}}{1 - r_{eh}^R r_{he}^L |r|^2}; \\ c_1 &= r^* + \frac{rr_{eh}^R r_{he}^L (t^2)^*}{1 - r_{eh}^R r_{he}^L |r|^2}; & c_2 &= r^* + \frac{rr_{eh}^L r_{he}^R (t^2)^*}{1 - r_{eh}^L r_{he}^R |r|^2}; & c_3 &= \frac{t^L_{hh} t^*}{1 - r_{eh}^L r_{he}^R |r|^2}; & c_4 &= \frac{t^R_{hh} t^*}{1 - r_{eh}^R r_{he}^L |r|^2}; \\ d_1 &= \frac{t^R_{hh} t^*}{1 - r_{eh}^R r_{he}^L |r|^2}; & d_2 &= \frac{t^L_{hh} t^*}{1 - r_{eh}^L r_{he}^R |r|^2}; & d_3 &= \frac{t^L_{hh} t^R_{hh} r^*}{1 - r_{eh}^L r_{he}^R |r|^2}; & d_4 &= \frac{t^R_{hh} t^L_{hh} r^*}{1 - r_{eh}^R r_{he}^L |r|^2}; \\ A_1 &= \frac{r_{he}^R |t|^2}{1 - r_{eh}^L r_{he}^R |r|^2}; & A_2 &= \frac{r_{he}^L |t|^2}{1 - r_{eh}^R r_{he}^L |r|^2}; & A_3 &= \frac{rr_{eh}^R t^L_{e\bar{e}} t^*}{1 - r_{eh}^L r_{he}^R |r|^2}; & A_4 &= \frac{rr_{eh}^L t^R_{e\bar{e}} t^*}{1 - r_{eh}^R r_{he}^L |r|^2}; \\ B_1 &= \frac{r_{he}^R tt^L_{\bar{H}H} r^*}{1 - r_{eh}^R r_{he}^L |r|^2}; & B_2 &= \frac{r_{he}^L tt^R_{\bar{H}H} r^*}{1 - r_{eh}^L r_{he}^R |r|^2}; & B_3 &= r_{\bar{h}\bar{e}}^L + \frac{r_{he}^L t^L_{e\bar{e}} t^L_{\bar{h}h} |r|^2}{1 - r_{eh}^L r_{he}^R |r|^2}; & B_4 &= r_{\bar{h}\bar{e}}^R + \frac{r_{he}^R t^R_{e\bar{e}} t^R_{\bar{h}h} |r|^2}{1 - r_{eh}^R r_{he}^L |r|^2}; \\ C_1 &= \frac{r_{eh}^R |t|^2}{1 - r_{eh}^L r_{he}^R |r|^2}; & C_2 &= \frac{r_{eh}^L |t|^2}{1 - r_{eh}^R r_{he}^L |r|^2}; & C_3 &= \frac{rr_{eh}^R tt^L_{\bar{H}H} r^*}{1 - r_{eh}^L r_{he}^R |r|^2}; & C_4 &= \frac{rr_{eh}^L tt^R_{\bar{H}H} r^*}{1 - r_{eh}^R r_{he}^L |r|^2}; \\ D_1 &= \frac{rr_{eh}^R t^L_{\bar{e}e} t^*}{1 - r_{eh}^R r_{he}^L |r|^2}; & D_2 &= \frac{rr_{eh}^L t^R_{\bar{e}e} t^*}{1 - r_{eh}^L r_{he}^R |r|^2}; & D_3 &= r_{\bar{e}\bar{h}}^L + \frac{r_{eh}^R t^L_{\bar{e}e} t^L_{\bar{h}h} |r|^2}{1 - r_{eh}^L r_{he}^R |r|^2}; & D_4 &= r_{\bar{e}\bar{h}}^R + \frac{r_{eh}^L t^R_{\bar{e}e} t^R_{\bar{h}h} |r|^2}{1 - r_{eh}^R r_{he}^L |r|^2}. \end{aligned} \quad (\text{S.11})$$

In Eq. (S.10) we have indicated with  $c_i^{\uparrow\downarrow}$  and  $b_i^{\uparrow\downarrow}$  the incoming and outgoing electrons and hole respectively with  $i = S_L, S_R, N$  labelling the corresponding lead. As an example of the derivation of the non-zero entries of the scattering matrix, let us explicit the calculation of the term  $a_1$ , which relates an incoming spin-up electron with an outgoing spin-up electron at the same  $N$  metallic lead

$$\begin{aligned} c_{N+}^\uparrow &\rightarrow c_{N-}^\uparrow : \\ a_1 &= r + tr_{he}^R r^* r_{eh}^L t + tr_{he}^R r^* r_{eh}^L r_{he}^R r^* r_{eh}^L t + \dots \\ &= r + t^2 r_{he}^R r^* r_{eh}^L \sum_{n=0}^{\infty} \left( r_{eh}^L r_{he}^R |r|^2 \right)^n \\ &= r + \frac{r_{eh}^L r_{he}^R t^2 r^*}{1 - r_{eh}^L r_{he}^R |r|^2} \end{aligned} \quad (\text{S.12})$$

## EVALUATION OF CURRENTS

As already mentioned in the main text (see Eq. (3)), the charge and heat currents can be written as [44]

$$J_i^k = \frac{2}{h} \sum_j \sum_{\alpha, \beta} (\alpha e)^{1-k} \int_0^\infty d\epsilon (\epsilon - \mu_i)^k \times \left( f_i^\alpha(\epsilon) - f_j^\beta(\epsilon) \right) P_{i,j}^{\alpha, \beta}(\epsilon),$$

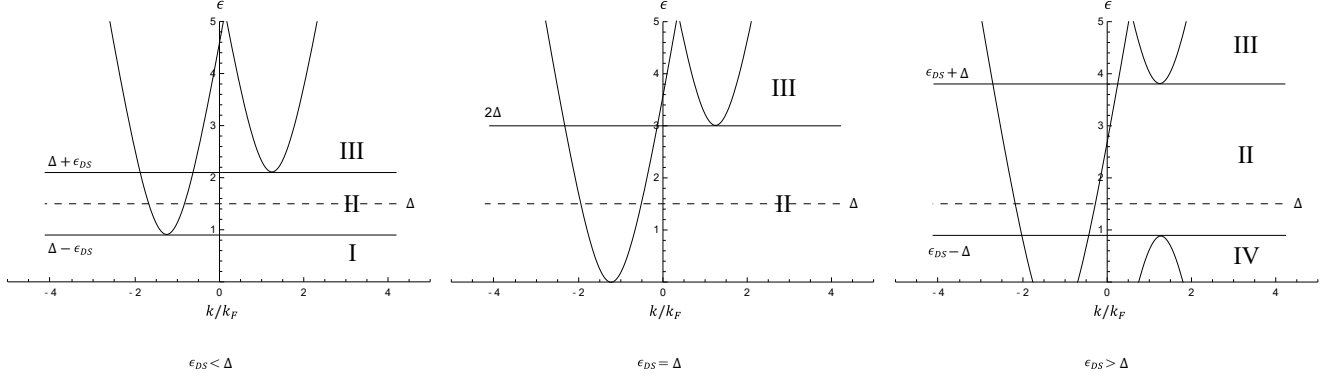


Figure 4. Regions of integration in Eq. (S.14) for  $\epsilon_{DS} > 0$ :  $\epsilon_{DS} < \Delta$  (left panel),  $\epsilon_{DS} = \Delta$  (middle panel),  $\epsilon_{DS} > \Delta$  (right panel).

where the scattering coefficients  $P_{i,j}^{\alpha,\beta}$  are defined as the trace over the channels  $a, b$ , i. e.

$$P_{i,j}^{\alpha,\beta}(\epsilon, \phi, \Phi) = \sum_{a,b} \left| S_{(i,a),(j,b)}^{\alpha,\beta} \right|^2, \quad (\text{S.13})$$

where we have made explicit the dependence on the phase difference  $\phi$  and the flux bias  $\Phi$ . Notice that  $P_{i,j}$  satisfies the time-reversal symmetry relations, namely  $P_{i,j}^{\alpha,\beta}(\epsilon, \phi, \Phi) = P_{j,i}^{\beta,\alpha}(\epsilon, -\phi, -\Phi)$  [44]. Finally Eq. (S.13) can be conveniently recast as follows

$$J_i^k = \frac{2e^{(1-k)}}{h} \left( \int_I j_{i,I}^k d\epsilon + \int_{II} j_{i,II}^k d\epsilon + \int_{III} j_{i,III}^k d\epsilon + \int_{IV} j_{i,IV}^k d\epsilon \right) \quad (\text{S.14})$$

where integrals are performed over the energy regions  $I, II, III$  and  $IV$  depicted in Fig. 4, which represent, respectively, the contributions deriving from the sub-gap (region I), the semi-continuum (region II) and the full continuum (regions III and IV). The full analytical expressions of the current integrands of Eq. (S.14) have been calculated, leading to some straightforward but cumbersome expressions that we do not report here for brevity.

### Charge current for weakly coupled probe

We can compute analytically the probe charge current  $J_N^0$  of Eqs. (S.14) in the lowest order in  $t$ , i.e. keeping the leading term in  $|t|^2$ . This represents a situation in which the probe is weakly coupled with the system and can be conveniently compared with the results computed with other methods such as the tunnelling approach (see later). The analytical expressions for the integrands of Eqs. (S.14) in this regime are given by:

$$j_{N,I}^0 = \mathcal{O}(|t|^4) \quad (\text{S.15})$$

$$j_{N,II}^0 = \left\{ \begin{aligned} & (f_N^+(\epsilon) - f_N^-(\epsilon)) \left[ \frac{\left( e^{4 \cosh^{-1}\left(\frac{|\epsilon_{DS}|+\epsilon}{\Delta}\right)} - 1 \right)}{-2e^{2 \cosh^{-1}\left(\frac{|\epsilon_{DS}|+\epsilon}{\Delta}\right)} \cos\left(\frac{2\epsilon_{DS}}{\epsilon_C} + \frac{2L(\epsilon_{DS}+\text{sgn}(\epsilon_{DS})\epsilon)}{\Delta} - \text{sgn}(\epsilon_{DS})\phi\right) + e^{4 \cosh^{-1}\left(\frac{|\epsilon_{DS}|+\epsilon}{\Delta}\right)} + 1} \right] + \\ & - (f_{S_R}^+(\epsilon) - f_{S_L}^-(\epsilon)) \frac{\left( e^{2 \cosh^{-1}\left(\frac{\epsilon_{DS}+\epsilon}{\Delta}\right)} - 1 \right)^2}{-2e^{2 \cosh^{-1}\left(\frac{\epsilon_{DS}+\epsilon}{\Delta}\right)} \cos\left(\frac{2\epsilon_{DS}}{\epsilon_C} + \frac{2L(\epsilon_{DS}+\epsilon)}{\Delta} + \phi\right) + e^{4 \cosh^{-1}\left(\frac{\epsilon_{DS}+\epsilon}{\Delta}\right)} + 1} \Theta(\epsilon_{DS}) \\ & - (f_{S_L}^+(\epsilon) - f_{S_R}^-(\epsilon)) \frac{\left( e^{2 \cosh^{-1}\left(\frac{-\epsilon_{DS}+\epsilon}{\Delta}\right)} - 1 \right)^2}{-2e^{2 \cosh^{-1}\left(\frac{-\epsilon_{DS}+\epsilon}{\Delta}\right)} \cos\left(\frac{2\epsilon_{DS}}{\epsilon_C} - \frac{2L(-\epsilon_{DS}+\epsilon)}{\Delta} + \phi\right) + e^{4 \cosh^{-1}\left(\frac{-\epsilon_{DS}+\epsilon}{\Delta}\right)} + 1} \Theta(-\epsilon_{DS}) \end{aligned} \right\} |t|^2 + \mathcal{O}(|t|^4) \quad (\text{S.16})$$

$$\begin{aligned}
j_{N,III}^0 = & \left[ (f_N^+(\epsilon) - f_N^-(\epsilon)) \left( \frac{2 \left( e^{2 \cosh^{-1} \left( \frac{\epsilon - \epsilon_{DS}}{\Delta} \right)} \cos \left( -\frac{2\epsilon_{DS}}{\epsilon_C} + \frac{2L(\epsilon - \epsilon_{DS})}{\Delta} - \phi \right) - 1 \right)}{-2e^{2 \cosh^{-1} \left( \frac{\epsilon - \epsilon_{DS}}{\Delta} \right)} \cos \left( -\frac{2\epsilon_{DS}}{\epsilon_C} + \frac{2L(\epsilon - \epsilon_{DS})}{\Delta} - \phi \right) + e^{4 \cosh^{-1} \left( \frac{\epsilon - \epsilon_{DS}}{\Delta} \right)} + 1} + \right. \right. \\
& \left. \left. + \frac{2 \left( e^{2 \cosh^{-1} \left( \frac{\epsilon_{DS} + \epsilon}{\Delta} \right)} \cos \left( \frac{2\epsilon_{DS}}{\epsilon_C} + \frac{2L(\epsilon_{DS} + \epsilon)}{\Delta} + \phi \right) - 1 \right)}{-2e^{2 \cosh^{-1} \left( \frac{\epsilon_{DS} + \epsilon}{\Delta} \right)} \cos \left( \frac{2\epsilon_{DS}}{\epsilon_C} + \frac{2L(\epsilon_{DS} + \epsilon)}{\Delta} + \phi \right) + e^{4 \cosh^{-1} \left( \frac{\epsilon_{DS} + \epsilon}{\Delta} \right)} + 1} + 2 \right) + \right. \\
& - (f_{S_R}^+(\epsilon) - f_{S_L}^-(\epsilon)) \frac{\left( e^{2 \cosh^{-1} \left( \frac{\epsilon_{DS} + \epsilon}{\Delta} \right)} - 1 \right)^2}{-2e^{2 \cosh^{-1} \left( \frac{\epsilon_{DS} + \epsilon}{\Delta} \right)} \cos \left( \frac{2\epsilon_{DS}}{\epsilon_C} + \frac{2L(\epsilon_{DS} + \epsilon)}{\Delta} + \phi \right) + e^{4 \cosh^{-1} \left( \frac{\epsilon_{DS} + \epsilon}{\Delta} \right)} + 1} + \\
& \left. - (f_{S_L}^+(\epsilon) - f_{S_R}^-(\epsilon)) \frac{\left( e^{2 \cosh^{-1} \left( \frac{\epsilon - \epsilon_{DS}}{\Delta} \right)} - 1 \right)^2}{-2e^{2 \cosh^{-1} \left( \frac{\epsilon - \epsilon_{DS}}{\Delta} \right)} \cos \left( -\frac{2\epsilon_{DS}}{\epsilon_C} + \frac{2L(\epsilon - \epsilon_{DS})}{\Delta} - \phi \right) + e^{4 \cosh^{-1} \left( \frac{\epsilon - \epsilon_{DS}}{\Delta} \right)} + 1} \right] |t|^2 + \mathcal{O}(|t|^4)
\end{aligned} \tag{S.17}$$

$$j_{N,IV}^0 \equiv j_{N,III}^0 \tag{S.18}$$

Here we consider the Fermi functions  $f_j^\alpha(\epsilon) = \{\exp[(\epsilon - \alpha\mu_j)/k_B T_j] + 1\}^{-1}$  of the leads  $j = S_L, S_R, N$  with  $\mu_N = eV_N$  and  $\mu_{S_R} = \mu_{S_L} = 0$  (i.e. superconductors are grounded); in the case in which the leads have independent temperatures  $T_N, T_{S_L}, T_{S_R}$  with  $T_N \lesssim \min(T_{S_L}, T_{S_R})$ , so that the heat flow between the probe and the TI does not affect neither the superconducting state of the contacts nor the proximitization with the TI. It is interesting to discuss some important experimental consequences which can be immediately derived by looking the previous expressions. We observe that the current integrands are factorised in terms of the Fermi function differences  $f_N^+(\epsilon) - f_N^-(\epsilon)$  and  $f_{S_L}^\pm(\epsilon) - f_{S_R}^\mp(\epsilon)$ . Notably, it can be shown that this happens not only in the opaque limit, but for every coupling with the probe (here we do not report the analytical expressions for brevity). As a consequence of this, there is no contribution from the Fermi function of the normal probe when  $V_N = 0$  since  $f_N^+(\epsilon) = f_N^-(\epsilon)$ . This clearly shows that, even in the non-linear regime, there is no thermoelectrical contribution induced by any thermal gradient between the probe and the TI edge since the probe temperature does not even appear in the expressions. The only contribution to the thermocurrent in the probe, instead, is purely nonlocal due to the application of a thermal gradient  $\delta T = T_{S_L} - T_{S_R}$  between the two superconductors; in which case the Fermi function differences  $f_{S_L}^\pm(\epsilon) - f_{S_R}^\mp(\epsilon)$  are not zero.

## COMPARISON WITH THE TUNNELLING APPROACH

In this section we compare the results obtained using the scattering approach with the results obtained using the tunneling approach [28–30, 32]. For the latter we use the formulation presented in Ref. [30], but modifying the density of states [Eq. (14)] by adding an imaginary part  $\gamma$  to the energy in order to phenomenologically capture the contribution of Andreev bound states.

### Charge current in the N probe

Let us now consider, regarding the scattering approach, the expression for the current  $J_N^0$  at lowest order in  $|t|^2$  derived in the previous section, and compare them with the results of the tunneling approach. In Figs. 5(a) and 5(b) we plot the current  $J_N^0$  and the differential conductance  $G_N = dJ_N^0/dV_N$ , respectively, as functions of the electrochemical potential  $eV_N$  for different values of  $\epsilon_{DS}$  and setting  $\gamma = 0$ . As expected, on the scale of the plot the curves relative to the two approaches coincide for both quantities. The density plot of the differential conductance  $G_N$  is also shown in Figs. 6(a) and 6(b) for the two approaches, respectively, as a function of  $eV_N$  and  $\epsilon_{DS}$ . Again, we see that the conductance  $G_N$  in the two approaches always coincides.

It is now important to notice that the expression for the current  $J_N^0$  in the scattering approach at lowest order in  $|t|^2$  do not describe the results of the tunnelling approach when a finite value of  $\gamma$  is taken. Indeed, in such a case  $G_N$  presents additional features produced by the ABSs [see Fig. 7(b), to be compared with Fig. 6(a)]. This is expected

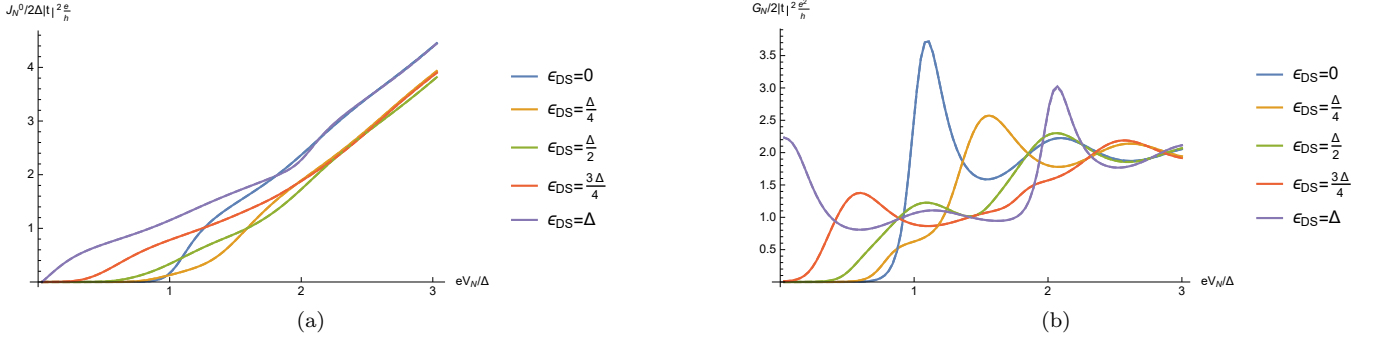


Figure 5. (a) - The charge current  $J_N^0$  at the metallic probe. Scattering results (solid lines) coincide with the tunneling ones (dashed lines), curves overlap. (b) - The differential conductance  $G_N$  at the metallic probe. Scattering results (solid lines) coincide with the tunneling ones (dashed lines), curves overlap. In both the plots we considered  $L/\xi = 3$ ,  $T/T_C = 1/10$  and  $\phi = 0$ .

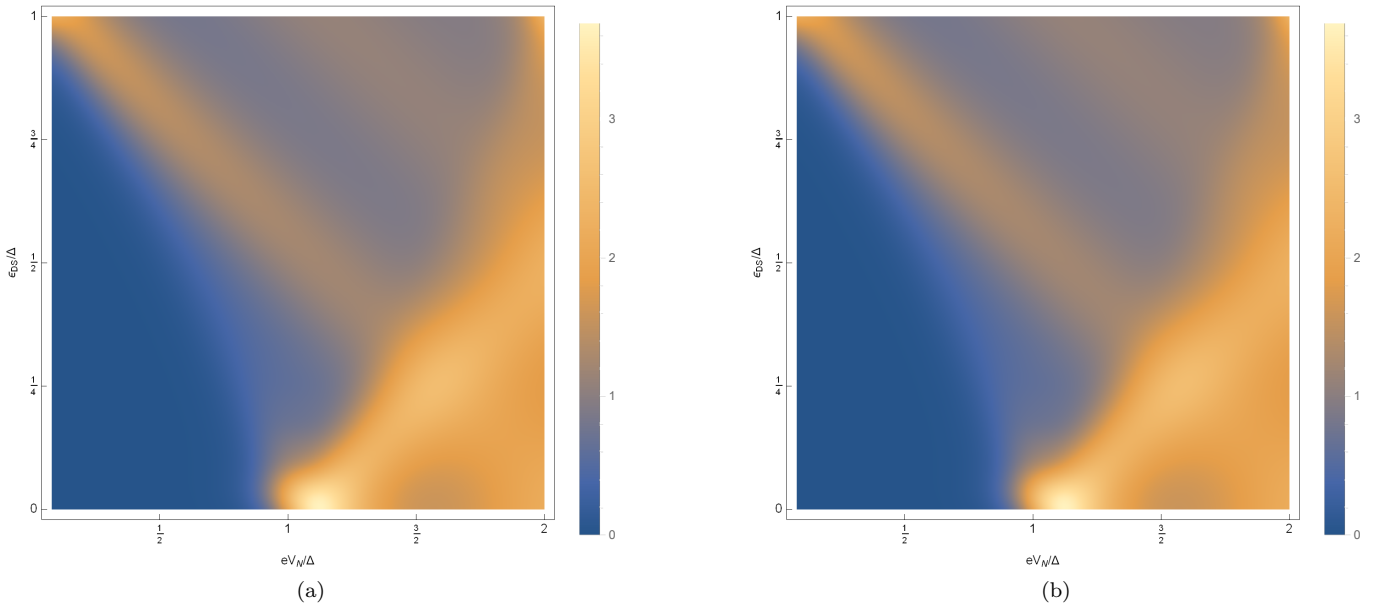


Figure 6. (a) - Density plot of the differential conductivity  $G_N$  at the metallic probe obtained with the scattering approach in the leading order in  $t$ . (b) - Density plot of the differential conductivity  $G_N$  at the metallic probe obtained with the tunneling approach with  $\gamma = 0$ . In both the plots we considered  $L/\xi = 3$ ,  $T/T_C = 1/10$  and  $\phi = 0$ .

because ABSs are accounted for by the scattering approach at the order  $\mathcal{O}(|t|^4)$ . By using the exact scattering approach one obtains the results reported in Fig. 7(a) for  $|t|^2 = 10^{-2}$ . By comparing the two panels of Fig. 7, we see that they show qualitatively the same behaviour (highlighting the presence of the ABSs in the same positions inside the gap), but they do not exactly match. The difference is due to the effective description of the tunnelling approach with respect to the exact scattering approach.

A more direct comparison between tunnelling approach and exact scattering approach is given in Fig. 8 where the linear-response conductance  $\sigma = L_{11}^L/T$  is plotted as a function of  $\epsilon_{DS}$  for various values of  $\phi$ . The two approaches almost exactly coincide apart from a dip in the peak at  $\phi = 0$  present in the tunneling curve (green dashed line).

We conclude the discussion by noting that only applying the full scattering formalism one can have a complete and consistent description of the transport in the three terminal setup which fully include the influence of ABSs. Similar considerations can be applied to the thermoelectrical current in the probe. In particular, we find that the scattering formalism shows, as naively expected, that ABSs do not contribute neither to thermal or to thermoelectrical current in the probe. One can analytically show that, at  $V_N = 0$ , there is no contribution to the N probe thermocurrent from ABSs for arbitrary values of  $|t|^2$ .

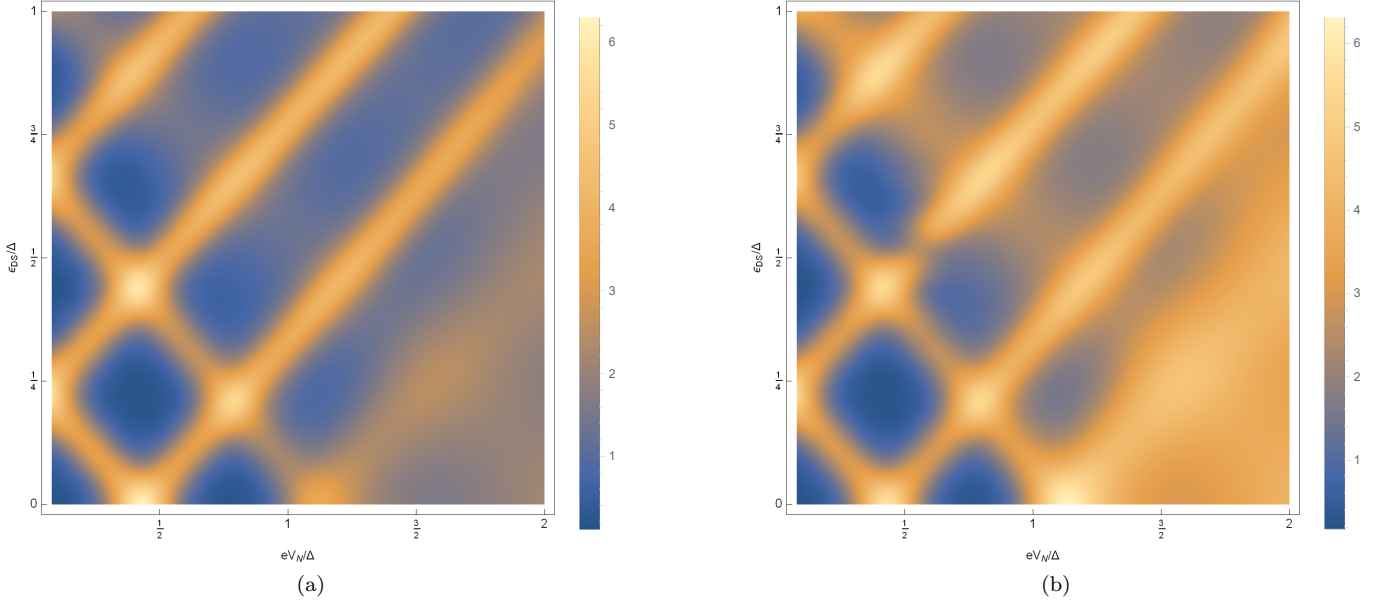


Figure 7. (a) - Density plot of the differential conductance obtained in the scattering approach.  $G_N$  is normalized with respect to the transmittance of the probe  $|t|^2 = 10^{-2}$ . (b) - Density plot of the differential conductance obtained in the tunneling approach. Here  $\gamma = \frac{\Delta}{1000}$ . In both the plots we considered  $L/\xi = 3$ ,  $T/T_C = 1/10$  and  $\phi = 0$ .

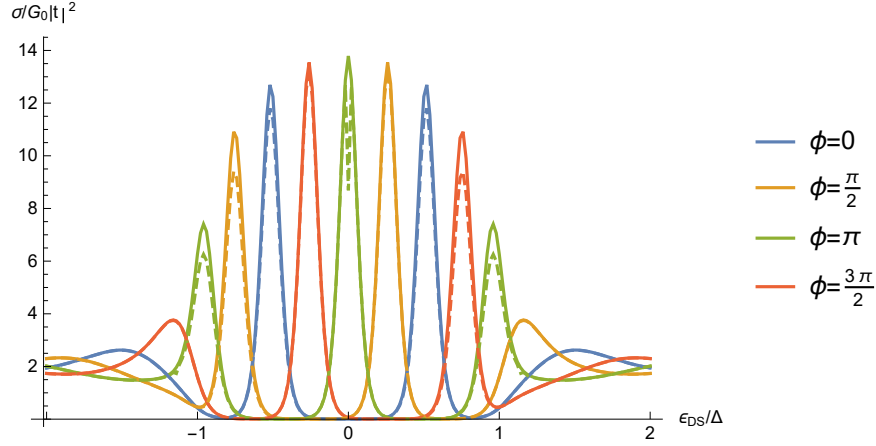


Figure 8. Linear regime - Scattering-Tunneling Comparison - Electrical conductance  $\sigma$  in units of  $G_0|t|^2$  (with  $G_0 = \frac{2e^2}{h}$  the electrical conductance quantum), as a function of  $\epsilon_{DS}/\Delta$ . Different curves refer to different values of the phase difference  $\phi$  between the two superconductors. Solid lines for the scattering approach (specifically  $|t|^2 = 10^{-2}$ ), dashed lines for the tunneling approach ( $\gamma = \frac{\Delta}{1000}$ ). The other parameters are:  $L/\xi = 3$ ,  $T/T_C = 1/10$  and  $\phi = 0$ .

### Thermal conductance without the probe

In this section is presented the thermal conductance  $\kappa = L_{22}^L/T^2$  calculated with the scattering approach by uncoupling the probe (i. e. setting  $t = 0$ ) and compared with the results of the tunneling approach. As expected the two approaches are completely equivalent: curves overlap for all the parameters - see Fig. 9.

### THERMOELECTRIC FIGURE OF MERIT $ZT$

Here we show the figure of merit  $ZT$  which parametrizes the maximum achievable efficiency  $\eta^{max} = \eta_C \frac{\sqrt{ZT+1}-1}{\sqrt{ZT+1}+1}$  (which approaches to the Carnot efficiency  $\eta_C = \delta T/T$  for  $ZT \rightarrow \infty$ ) in the linear regime when the device is regarded

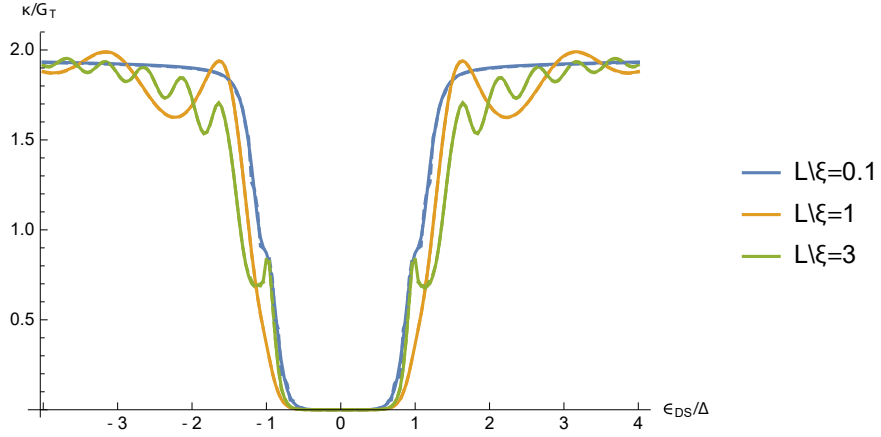


Figure 9. Linear regime - Comparison between the scattering approach (without the probe) and tunneling method calculated using the DOS [29] - Thermal conductance  $\kappa$  in units of the thermal conductance quantum  $G_T = \frac{\pi^2}{3h} k_B^2 T$ , as a function of  $\epsilon_{DS}/\Delta$ . Different curves refer to different values of  $L/\xi = 1/10, 1, 3$ . Solid lines for the scattering approach, dashed lines for the results obtained using the DOS [29]: curves exactly overlap. Other parameters:  $T/T_C = 1/10$  and  $\phi = 0$ .

as a thermoelectric heat-engine/refrigerator. In our case this is defined as  $ZT = -\frac{L_{12}L_{21}}{L_{11}L_{22}}$  since  $L_{12} = -L_{21}$ . We plot  $ZT$  in Fig. 10 as a function of  $\epsilon_{DS}$  and  $|t|^2$  for the parameters specified in the caption. We notice that the value of  $ZT$  is non zero only for  $\epsilon_{DS} \sim \pm\Delta$  (where the Seebeck is maximal). Interestingly the  $ZT$  is maximal for  $|t|^2 = 1$ , i.e. in the regime of maximum coupling with the probe, but reaching quite small values  $\sim 0.1$ . In this respect we notice that a coupling with the normal probe containing an additional energy filter like a quantum dot would lead to higher values.

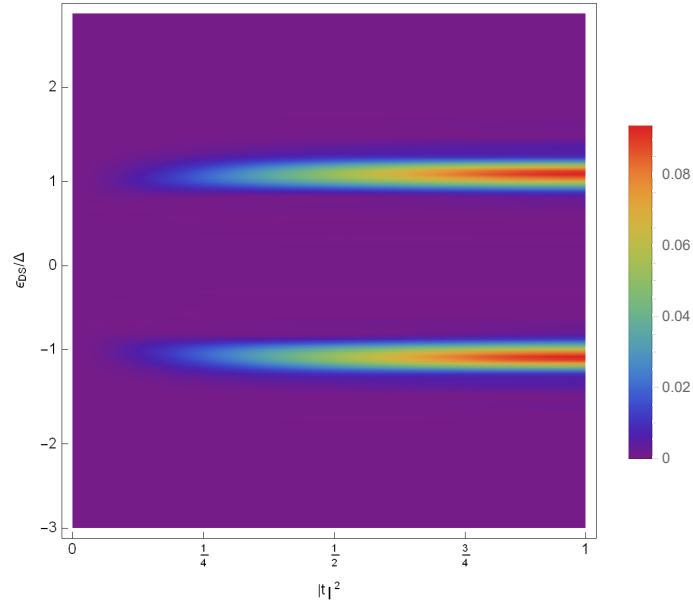


Figure 10. Density plots of the figure of merit  $ZT$  plotted as a function of  $\epsilon_{DS}/\Delta$  and  $|t|^2$ . The parameters used are:  $L/\xi = 1$ ,  $T/T_C = 1/10$  and  $\phi = 0$ .